ACS OMEGA

Open Access

http://pubs.acs.org/journal/acsodf

Article

A Nickel-Based Semiconductor Hybrid Material with Significant Dielectric Constant for Electronic Capacitors

Dhouha Abid, Issam Mjejri, Abderrazek Oueslati, Philippe Guionneau, Stanislav Pechev, Nathalie Daro, and Zakaria Elaoud*

Cite This: *ACS Omega* 2024, 9, 12743−12752

Read Online

ACCESS | Metrics & More | Article Recommendations | Supporting Information

ABSTRACT: A novel semiconducting Ni(II)-based hybrid material with the formula $(C_7H_{12}N_2)$ $NiCl_4$, which exhibits interesting optical and electrical properties, is reported. The crystal structure was investigated using SCXRD, whereas physical properties were studied by means of thermal analysis, Ft-Infrared, optical, and electrical measurements. Its crystal packing is formed through organic rings surrounded by inorganic $[NiCl_4]^{2-}$ tetrahedral and stacked along the *a*-crystallographic axis. This arrangement is stabilized by a dense network of intermolecular hydrogen bonds. The investigated compound displayed a wide absorption range across the visible spectrum, characterized by an optical gap energy of 2.64 eV, indicating its semiconducting nature and efficient sunlight absorption capabilities across various wavelengths. Such features are of utmost importance in achieving a high energy conversion efficiency in solar cell applications. Further analyses of the thermal behavior using differential scanning calorimetry revealed a single-phase transition occurring at around 413 K, which was further confirmed through electrical measurements. A deep investigation of the electric and dielectric performances demonstrated a significant dielectric constant ($\varepsilon' \sim 10^4$) at low frequencies and low dielectric loss at high frequencies. Thus, it highlights its exceptional dielectric potential, particularly in applications related to electronic capacitors.

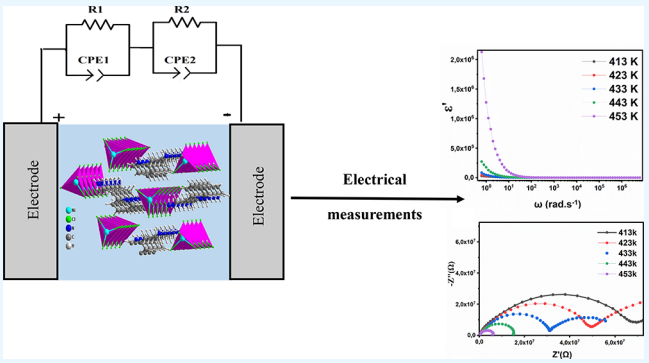

1. INTRODUCTION

In our pursuit of a sustainable future, electronic capacitors have emerged as fundamental building blocks of modern electronic systems, revolutionizing various aspects of our daily lives. These versatile components have played a crucial role in advancing technology and enabling the development of highly integrated circuits, efficient energy systems, and sophisticated electronic devices. Electronic capacitors have become crucial in a variety of electronic devices that have become essential to our modern society, such as computers, smartphones, and even integrated circuits.[1−6]

Significant progress has been made in the field of capacitors through the development of semiconducting materials such as silicon,[7,8] graphene,[9,10] carbon nanotubes,[11,12] and so on. Among these new materials, hybrid compounds have demonstrated exceptional physical properties, including tenability, high electron mobility, low thermal conductivity, improved performance, and lower production costs. These materials offer the advantage of incorporating, within the same atomic architecture, both organic and inorganic properties. This combination results in multifunctional materials that integrate useful properties within a single composite, opening up a broad range of technological applications.[13−16]

The unique characteristics of halide-based hybrid materials have sparked considerable interest in their potential in various fields. Their remarkable properties have paved the way for advancements in electronics and other technological domains and opened new frontiers in light detectors, quantum computing, and memory devices.[14−21] Aside from these fascinating electrical characteristics, these crystalline materials have exhibited compelling optical properties, expanding the range of potential applications, especially in optoelectronics and photovoltaic solar cells.[22−27] By taking advantage of the physical properties of the different entities that form hybrid materials, researchers are exploring new frontiers in the development of advanced systems.[28−33]

In 2023, A.Ghoudi's group synthesized a 0D hybrid material with the formula $C_6H_9N_2FeCl_4$.[34] The semiconducting nature of this compound was verified through optical-absorption measurements, revealing a band gap of approximately 2.47 eV.

Received: October 27, 2023
Revised: February 1, 2024
Accepted: February 9, 2024
Published: March 8, 2024

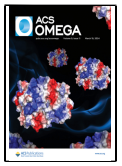

At low frequencies, this material exhibits a notable dielectric constant, reaching values of around 10^6, which signifies that the synthesized material is a good candidate for electrical energy storage applications.

Within this context, our research groups designed, in 2023, a low-dimensional and eco-friendly Ni(II)-based hybrid material, namely $[(C_3H_7)_4N]$ Ni_2Cl_6[35] that demonstrated interesting semiconducting properties with an optical gap energy of 3.72 eV, making it an excellent candidate for photovoltaic applications, particularly in solar cell technology. The reported $(H_2AMP)_2[Fe^{III}Br_4]$ Br_3[36] (AMP: 2-(ammoniomethyl)-pyridinium) hybrid material revealed an optical band gap of 1.06 eV, which promoted efficient energy conversion processes. In 2021, R. Kalthoum and coauthors reported two hybrid materials, (CH_3NH_3) $CdCl_3$ and $(CH_3)_2NH_2CdCl_3$,[37] that demonstrated good electric properties for capacitor devices with dielectric constants, reaching values of 10^3 at low frequencies and high electrical conductivity of approximately 2.10^{-4} $S.m^{-1}$, along with a low dielectric loss of less than 0.1 at high frequencies. While some halide-based hybrid materials are ideal for use in electronic devices, they face limitations due to their low dielectric constants and the instability of their molecular frameworks during electrical measurements, which limit their application in certain systems.

In continuation of the above groundbreaking research efforts aimed at improving these findings, we report a novel semiconductor Ni(II)-based hybrid compound with the formula $(C_7H_{12}N_2)$ $NiCl_4$. Its crystal structure, thermal (TGA and DSC) profiles, and spectroscopic features were studied. Additionally, the synthesized hybrid material was optically and electrically evaluated in order to gain insights into the semiconducting properties and electric mechanisms as well as to confirm the phase transition observed in thermal analysis.

2. EXPERIMENTAL SECTION

Chemical reagents, including 2-(2-aminoethyl) pyridine ($C_7H_{10}N_2$, 95%) and nickel(II) chloride hexahydrate ($NiCl_2.6H_2O$, 99%), were acquired from a commercial source (Sigma-Aldrich) and used as received without purification.

2.1. Sample Preparation. Green crystals of $(C_7H_{12}N_2)$ $NiCl_4$ were obtained through the slow evaporation technique of an aqueous solution containing 2-(2-aminoethyl) pyridine and nickel chloride hexahydrate in 1:2 molar ratios at room temperature. The reactants were dissolved in a small amount of distilled water and stirred briefly, while hydrochloric acid (HCl) was gradually added dropwise to it. After 1 week, the crystals were collected via filtration and air-dried.

2.2. Instruments. *2.2.1. Single Crystal X-ray Diffraction.* A suitable crystal of Ni(II) halide-based material was chosen and examined under a polarizing microscope before being mounted on a Bruker APEX II diffractometer with Mo−Kα radiation. The data collected spanned an angular range of $1.9° \leq \theta \leq 30.2°$, and a total of 40027 reflections were recorded, among which 2893 reflections had an intensity of $I > 2\sigma(I)$.

The crystal structure was solved in the monoclinic system with the space group $P2_1/c$ using the SHELXS-97[38] program within the WINGX software.[39] Nickel atoms were fixed with the Patterson method, while other atoms were found through Fourier calculations and refined using the SHELXL-2018[40] program with anisotropic thermal parameters. Hydrogen atoms were positioned by using a riding model. After several refinements, the final reliability factors are R_1 = 0.032, and wR_2 = 0.071. The Diamond program[41] was used to draw packing figures.

Table S1 gathers the crystallographic details of the structure refinement process for the Ni(II)-hybrid material. Tables S2 and S3 provide atomic positional parameters and anisotropic factors, respectively. Interatomic distances and bond angles are listed in Table S4.

2.2.2. TGA-DSC Measurements. The sample weighing 2.351 mg was carried out for thermogravimetric analysis (TGA) under an oxygen atmosphere with a linear heating rate of 10 °C/min. The analysis was carried out within a temperature range of 303−773 K. Additionally, a differential scanning calorimetry (DSC) measurement was conducted on a sample weighing 5800 mg using a "DSC 822P METTLER TOLEDO" type device. The measurement was performed at a heating rate of 10 °C/min within a temperature range of 243−623 K.

2.2.3. Thin-Film Preparation. The spin-coating technique was used to prepare the Co(II)-based material's thin film. The crystals were spin-coated onto a solid quartz substrate for 10 s at a speed of 2500 rpm after being dissolved in 1 mL of distilled water. An annealing process at 80 °C was used to remove any residual solvent from the resultant film.

Using spin-coated sheets, optical-absorption measurements (OA) of the sample were performed at room temperature using a standard UV−vis spectrophotometer (HITACHI, U3300).

2.2.4. Electrical Measurements. Electrical measurements were conducted on a polycrystalline sample by forming it into a pellet using a uniaxial hydraulic press. The resulting pellet had a diameter of approximately 8 mm and a thickness of 1.3 mm. The pellet was then positioned between two platinum electrodes. The complex impedance spectra were subsequently recorded within a frequency range spanning from 1 Hz to 1 MHz using a TEGAM 3550 ALF automatic bridge. The measurements were performed while gradually heating the sample from 333 to 453 K.

3. RESULTS AND DISCUSSION

3.1. Crystallographic Features. The SCXRD study reveals that the investigated compound crystallizes in centrosymmetric space group $P2_1/c$, featuring a 2D framework in the sense that the crystal packing is made of discrete entities of $C_7H_{12}Cl_4N_2$ and $NiCl_4$. As reported in Figure S1, the asymmetric unit is composed of a diprotonated 2-(2-aminoethyl) pyridine group and one $[NiCl_4]^{2-}$ tetrahedron. We noticed that all atoms occupy a general position with a Wyckoff site of (4e). The projection of the crystal structure, as presented in Figure 1a, reveals an infinite pseudolayers comprising $[NiCl_4]^{2-}$ anions and organic groups, both linked by a network of hydrogen bonds to confer a 2D character to the intermolecular interaction topology. The nickel atom exhibits tetrahedral coordination, surrounded by four chlorine atoms, conferring a slightly distorted tetrahedron (inset of Figure 1b).

The average values of the axial Ni−Cl bond length are 2.269(6) Å, while the equatorial Ni−Cl bond lengths range from 2.272(7) to 2.274(6) Å. The Cl−Ni−Cl bite angles vary between 105.78(2) and 113.72(2)°. These values are in good agreement with those observed in the $[(C_3H_7)_4N]$ Ni_2Cl_6[35] perovskite compound, where the Ni−Cl bond distances are in the range 2.205(5) and 2.324(5) Å and the Cl−Ni−Cl bond angles range from 85.55(19) to 147.67(3)°. It is worth noting that the $[NiCl_4]^{2-}$ groups are separated by a minimum

https://doi.org/10.1021/acsomega.3c08499
ACS Omega 2024, 9, 12743−12752

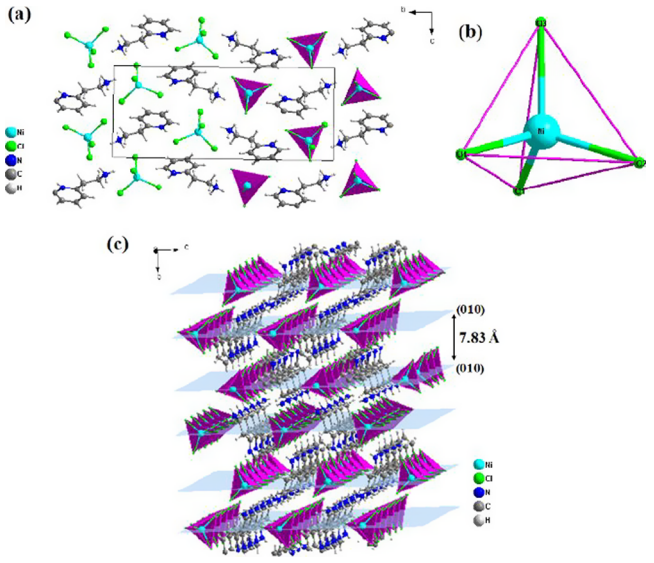

Figure 1. (a) Coordination sphere of the $[NiCl_4]_{2-}$ tetrahedron, (b) projection of the organic layers and inorganic polyhedron along the crystallographic *a*-axis, and (c) perspective view of the [011] plans comprising $[NiCl_4]_{2-}$ anions and organic ions.

intermetallic distance of Ni−Ni = 8.40(3) Å, indicating the absence of magnetic interactions between the metal centers. It is to be noticed that the organic−inorganic layers are stacked in the [011] planes with an interplane distance of 7.836 A (Figure 1c). Bond distances and angles are similar to those previously reported for nickel-based compounds.[42−45]

By considering the geometrical properties, the calculated average distortion index for the Ni (II) atom is ID $_{d(M-L)}$ = 0.0034. This parameter (DI) is determined using the following formula:[46]

$$ID_{d(M-L)} = \sum_{i=1}^{4} \frac{[d_i - d_m]}{4d_m} \quad (1)$$

where d_m and d_i values present the average distances and the values of the distances of the metal−ligand bonds (Ni−Cl), respectively.

The organic rings are located at y = 1/4 and y = 3/4. The values of the N−C and C−C bond lengths are in the ranges of 1.342 (3)−1.488 (3), and 1.367 (3)−1.517 (3) Å, respectively. These average values are in accordance with those observed in similar compounds based on the organic 2-(2-aminoethyl) pyridine group.[47−50] The interatomic distances and bond angles are listed in Table S4. We noticed that the crystal structure packing is stabilized through intermolecular C−H···Cl and N−H···Cl hydrogen bonds between organic groups and inorganic $[NiCl_4]^{2-}$ tetrahedral. The C−H···Cl distances vary from 3.437 (2) to 3.848 (2) Å, while the N−H···Cl distances are between 3.176 (2) and 3.383 (2) Å.

These various intermolecular hydrogen interactions give birth to a 2D framework. All hydrogen bonds are gathered in Table S5.

3.2. Thermal Stability. The crystal structure stability of the investigated sample was confirmed using TGA-DSC measurements. The TGA analysis presented in Figure 2 shows that the initial weight loss, occurring between 300 and 367 K and accounting for a mass loss of 18%, is attributed to the removal of adsorbed water molecules due to the hygroscopic nature of the sample. A similar phenomenon

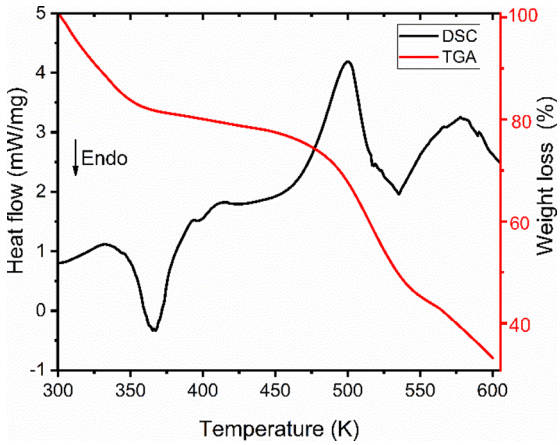

Figure 2. TGA (red line)-DSC (black line) spectra of the Ni(II)-based compound.

was observed for $[N(C_3H_7)_4]_2Ni_2Cl_6$.[35] The two subsequent mass losses observed between 437 and 600 K are associated with the decomposition of the polymeric network, resulting in the formation of NiO as the final residue at 598 K.

The DSC thermogram displays several distinct peaks. The first endothermic peak, observed at approximately 364 K, corresponds to the removal of adsorbed water molecules, which is attributed to the compound's hygroscopic nature. The second exothermic peak, located at around 413 K, is assigned to the phase transition of the sample. Finally, peaks around 498 and 580 K indicate the fusion of the title compound, followed by the subsequent decomposition of its polymeric network.

3.3. Optical Investigation. The room-temperature optical properties of the $(C_7H_{12}N_2)$ $NiCl_4$ compound were investigated by recording its UV−visible absorption spectrum in the range of 280−750 nm. Figure 3a shows the normalized

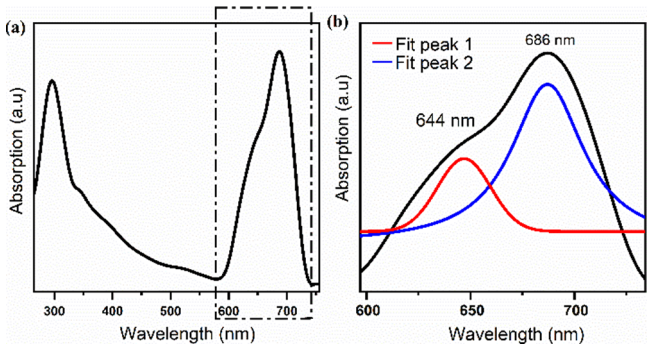

Figure 3. (a) Normalized absorption spectrum of the $(C_7H_{12}N_2)$-$NiCl_4$ title compound. (b) The deconvolution of the optical spectrum between 500 and 750 nm.

absorption spectrum, which exhibits a sharp peak around 296 nm, followed by a shoulder peak at 346 nm. Based on previously reported hybrid Ni(II)-based materials, the higher-energy peak at around 296 nm is attributed to the ligand-to-metal charge transfer (LMCT) excited state. On the other hand, the lower-energy peak at 346 nm can be assigned to the (MC) transition, which occurs when an electron is excited from the valence band comprising the 3p orbital of the chlorine atom to the conduction band comprising the $4s^2$ orbital of the nickel atom.[51−53]

https://doi.org/10.1021/acsomega.3c08499
ACS Omega 2024, 9, 12743−12752

The deconvolution of the normalized optical spectrum (Figure 3b) in the spectral region between 500 and 750 nm reveals the presence of a shoulder peak with a maximum intensity at 644 nm, followed by a Gaussian-shaped peak at 686 nm. These features are associated with the d-d electronic transitions within the Ni^{2+} ion. Based on the Tanabe-Sugano diagram for the Ni(II) tetrahedron, two spin-allowed bands are expected. The first peak at 637 nm is associated with the transition from the $^3A_2$ (3F) ground term to the $^3E(3F)$ excited state, while the second peak at around 668 nm is assigned to transitions from $^3A_2(3F)$ ground term to the $^3E(3P)$.[54]

The optical gap energies for the Ni(II)-based hybrid material ($E_{g(d)}$ and $E_{g(ind)}$) were determined using Tauc's expression:

$$(\alpha h\nu) = B(h\nu - E_g)^n \quad (2)$$

where B is constant, E_g: the gap energy, and n: constant that defines the type of optical transition ($n = 1/2$ for the direct transition and $n = 2$ for the indirect transition).

The absorption coefficient α can be determined through the following relationship:

$$\alpha = (2.3003A)/d \quad (3)$$

where A and d represent the absorbance and the thickness of the cuvette, respectively.

The direct and indirect gap energies were determined by extrapolating the linear part of the curve to the energy-axis. Figure 4a,b depicts the dependence of $(\alpha h\nu)^{1/2}$ and $(\alpha h\nu)^2$ on

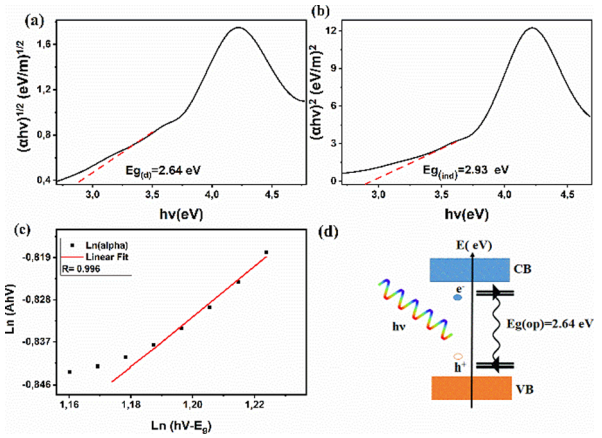

Figure 4. Plot of (a) $(\alpha h\nu)^{1/2}$ and (b) $(\alpha h\nu)^2$ versus $(h\nu)$, (c) dependence of $\ln(h\nu - E_{op})$ as a function of $\mathrm{Ln}(Ah\nu)$, and (d) diagram the optical-absorption (OA) process within the synthesized $(C_7H_{12}N_2)$ $NiCl_4$ title compound.

the photon energy $h\nu$. Through this analysis, the direct and indirect gap energies were estimated to be 2.64 and 2.93 eV, respectively. In order to determine the optical gap energy E_g (op) of the title compound, a precise method was employed using the following formula:

$$n = (\ln(\alpha h\nu)\ln)/(h\nu - E_{op}) \quad (4)$$

By analysis of the $\ln(h\nu - E_{op})$ versus $\ln(Ah\nu)$ plot in Figure 4c, the slope of the curve is determined to be 0.91. This value confirms a directly allowed transition in the title compound (inset of Figure 4d). Based on these findings, the Ni(II)-based material can be classified as a semiconductor and can effectively absorb sunlight across a wide range of wavelengths. This property is crucial for efficient energy conversion in solar cells, as it allows the material to harness a significant portion of the solar spectrum.[55−57]

3.4. Electrical Properties. *3.4.1. Impedance Complex and Equivalent Circuit Analysis.* In order to provide valuable insight into the electrical processes and the conduction mechanism occurring within the Ni-based system, electrical properties were examined using complex impedance spectroscopy in the range 333−453 K. Figure 5a shows the Nyquist

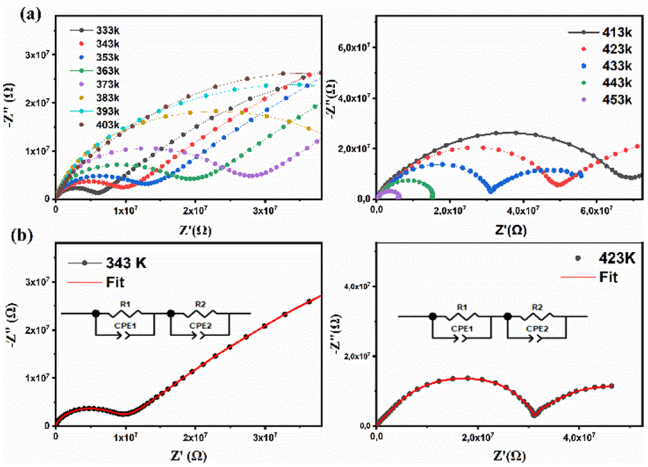

Figure 5. (a) Nyquist plots (Z' versus Z'') at various frequencies and temperatures for the investigated Ni(II)-based compound, (b) plots of the fitted impedance complex diagram at 343 and 423 K and their representative equivalent circuit.

plots (Z' versus Z'') at various temperatures. The impedance spectra exhibit some dispersion rather than a semicircle that were centered on the real axis. This dispersion indicated a non-Debye (Cole−Cole) type of relaxation. Below T = 413 K, the radius of the semicircle increased as the temperature rose. This behavior suggests a decrease in thermal conductivity. The following process is mainly attributed to the presence of adsorbed water molecules, which is confirmed through TGA measurements. In fact, the water molecules tend to infiltrate the grain boundary pores and act as trapping centers for charge carriers. This phenomenon is commonly observed in organic−inorganic-halide-based materials.[58]

At higher temperatures (above 413 K), the Nyquist diagrams displayed a decrease in the radius of the semicircle with an increase in temperature. This trend provides clear evidence of an activated conduction process in the material, indicating enhanced conductivity as the temperature increases.[14,19,59]

The impedance spectra plots were successfully fitted using an equivalent circuit model consisting of a combination of pure resistance (R_1) and a fractal capacitor (CPE_1) in series with a second pure resistance (R_2) and a fractal capacitor (CPE_2). The fractal capacitance (CPE) is given by the following expression:

$$Z_{CPE} = \frac{1}{Q_0(j\omega)^{\propto}} = \frac{1}{(Q\omega^{\propto})\cos\left(\frac{\propto \pi}{2}\right)} + \frac{1}{(jQ\omega^{\propto})\sin\left(\frac{\propto \pi}{2}\right)} \quad (5)$$

The obtained results demonstrate excellent agreement between the experimental data and calculated values, providing

https://doi.org/10.1021/acsomega.3c08499
ACS Omega 2024, 9, 12743−12752

compelling evidence that the proposed equivalent circuit effectively describes the electrical behavior of the investigated material (Figure 5b).

The frequency-dependent variation of the real part (Z') of the complex impedance at different temperatures is depicted in Figure 6a. Notably, at lower temperatures, the amplitude of Z'

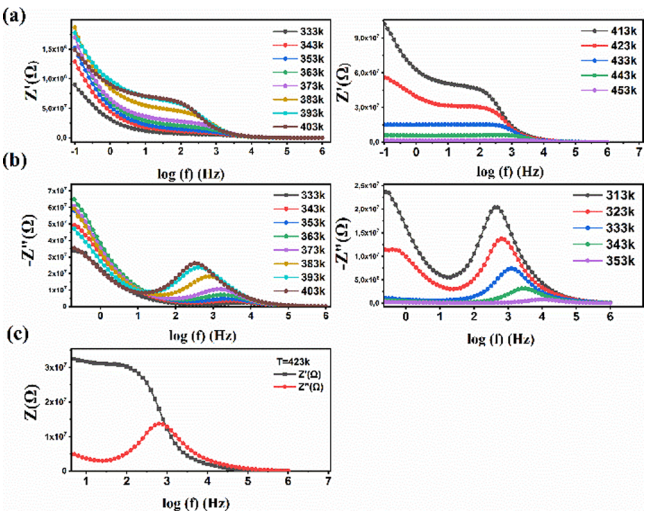

Figure 6. Frequency-dependent variation of the real part (a) (Z') and (b) (Z'') of the complex impedance at different temperatures. (c) Variation of frequency as a function of the real and imaginary parts of the impedance complex (Z' and Z'') at 423 K.

is significantly higher in the low-frequency region and then gradually decreases as both temperature and frequency increase. This behavior points to enhanced DC conductivity in the title compound.

Furthermore, in the high-frequency range, all the curves converge, with Z' becoming independent of frequency. This convergence suggests the liberation of charge carriers and a subsequent reduction in barrier properties within the sample.[60,61]

A close look at the variation of Z'' versus frequency plot (Figure 6b) shows that Z'' increases as temperature and frequency rise until reaching a maximum value Z''_{max}, then it gradually decreases. The broadening of peaks indicates the occurrence of a relaxation process within the system.[61] As the frequency decreases, all of the curves converge, indicating a potential release of charge carriers. In fact, at higher frequencies, the charge carriers have less time to relax, resulting in a decrease in polarization with increasing frequency. This behavior leads to a fusion of the curves.[62−64]

Figure 7c illustrates the variation of the frequency as a function of the real and imaginary parts of the impedance complex (Z' and Z'') at 423 K. Notably, Z'' increases with frequency, while Z' decreases. This trend continues until Z'' reaches its maximum value (Z''_{max}) and intersects with the Z' plot. As the frequency further increases, both Z' and Z'' decrease until they reach zero.[65]

The temperature dependence of the conductivity is presented in Figure 7, where two regions are observed: one at T > 413 K and another at T < 413 K, with a noticeable change in the slope around 413 K, confirming the phase transition observed in the DSC measurements. The curve also demonstrates an increase in conductivity with rising temperatures. These findings suggest that the conduction in the

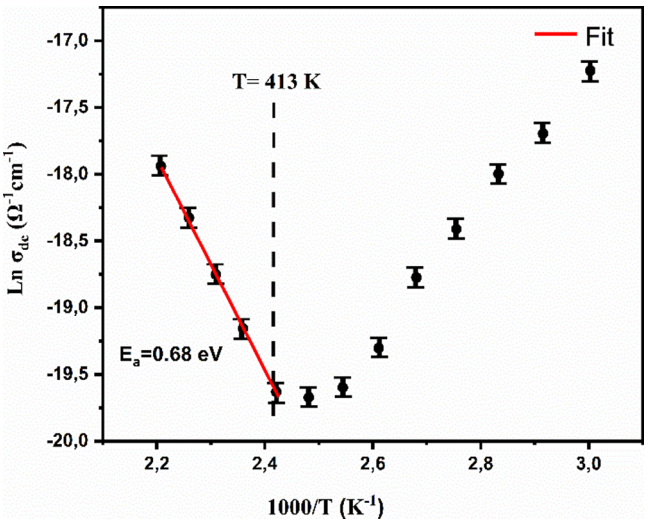

Figure 7. Variation of DC conductivity as a function of temperature.

compound follows a thermally activated transport process governed by the Arrhenius law:

$$\sigma_{dc}T = \sigma_0 \exp(-E_a/k_B T) \quad (6)$$

where; σ_0, E_a, and k_B, represent the pre-exponential term, activation energy, and Boltzmann constant, respectively.

In region II, the activation energy is determined to be E_a (II) = 0.68 eV, indicating that the investigated compound is classified as a semiconductor material.

3.4.2. AC Conductivity. In order to study the dynamic response of the material to an applied alternating electric field, an investigation of the alternating current conductivity was conducted.

The conductivity, σ_{ac}, was calculated using the following equation:

$$\sigma_{ac} = \left(\frac{e}{s}\right)\left(\frac{Z'}{Z'^2 + Z''^2}\right) \quad (7)$$

The alternative AC conductivity is displayed as σ_{ac} vs log f (Figure 8). It is observed that the conductivity, σ_{ac}, increases

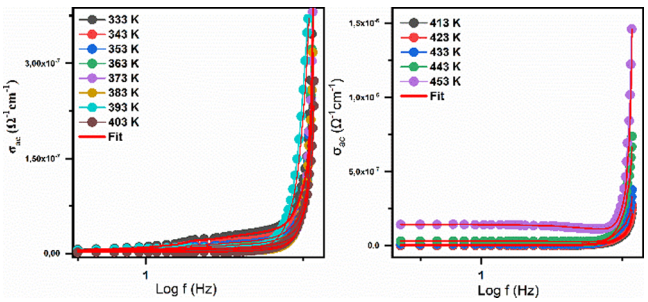

Figure 8. Variation of the alternative AC conductivity as a function of frequency for the investigated ($C_7H_{12}N_2$) $NiCl_4$ perovskite material.

with increasing temperature. Upon closer examination of the conductivity plots, two distinct regions are observed: the first region, at low frequencies, exhibits a plateau of direct current conductivity σdc, while the second region, observed at high frequencies, shows a dispersion due to interactions between charge carriers.[66] The phenomenon of conductivity dispersion, σac, can be described by the Jonscher law:[67]

https://doi.org/10.1021/acsomega.3c08499
ACS Omega 2024, 9, 12743−12752

$$\sigma_{ac} = \sigma_{dc} + A\omega^{s} \quad (8)$$

where; σ_{dc} is the DC conductivity, A: a constant that depends on the temperature, S: a parameter that measures the degree of interaction between mobile ions and its surroundings. This parameter is in the range of $[0-1]$, and ω is the angular frequency.

The plot of the exponent 's' (Figure 9) provides valuable information about the conduction mechanism. The plot reveals

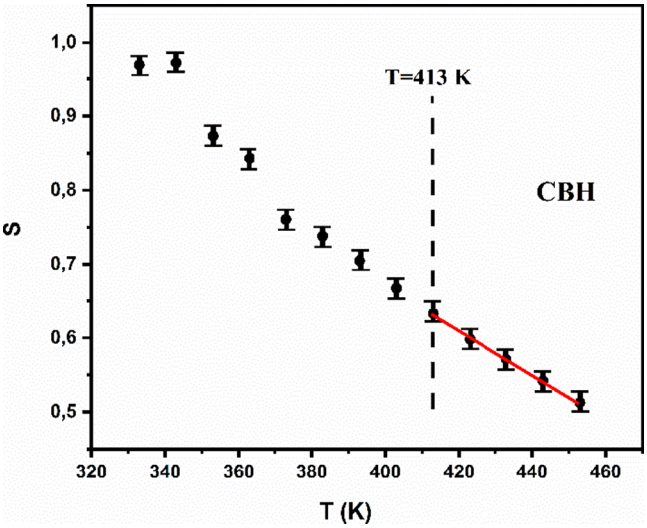

Figure 9. Plot of the exponent 's' versus temperature for the investigated nickel-based compound.

that above 413 K, the exponent 's' decreases as the temperature increases. This behavior indicates that the electrical transport process in the material is governed by the correlated barrier hopping (CBH) model.

3.4.3. Modulus Analysis. The complex modulus formalism provides insight into the electrode polarization conductivity and relaxation behavior. It serves as a valuable technique for comprehending the material's transport process and relaxation mechanism.

The complex electric modulus M^* is defined by the following equations:

$$M^* = i\omega C_0 Z^* = M' + j \quad (9)$$

where; C_0 is the capacitance vacuum. M', M'': present, respectively, the real and imaginary parts of the complex electrical modulus M^*.

In order to investigate the contribution of these phenomena, we have studied the variation of the real part M' of the complex modulus at different frequencies and temperatures (Figure 10a). Notably, at low frequencies, the values of M' were found to be very low, indicating that the influence of the electrodes is negligible. In this low-frequency region, the value of M' initially decreases and then gradually rises with increasing frequency. This behavior can be attributed to the fact that the electric field generated is not strong enough to provide the necessary restoring force for the movement of the charge carriers. As a result, the conduction process is primarily driven by the short-range mobility of the charge carriers. At high frequencies, M' approaches a constant value ($M'_{\infty} = 1/\varepsilon'_{\infty}$), which indicates the presence of a relaxation process within the investigated Ni (II)-based material.[68,69]

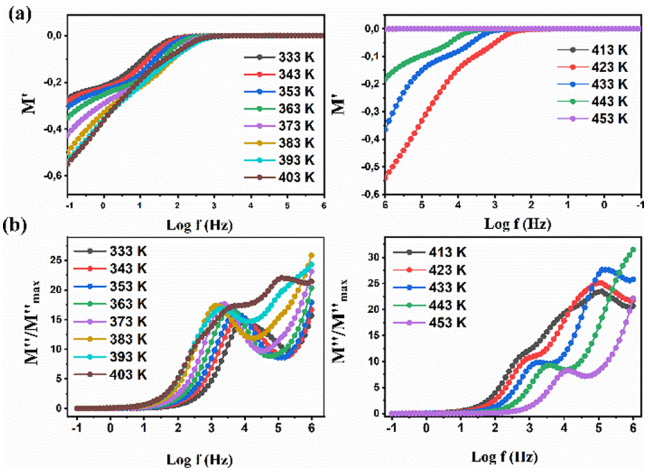

Figure 10. Variation of (a) the real part M' of the complex modulus and (b) the normalized imaginary part M''/M''_{max} versus $\log(f)$ at different temperatures.

The 2D plots depicting the variation of the normalized imaginary part M''/M''_{max} versus $\log(f)$ for different temperatures are shown in Figure 10b. These curves appear as asymmetric relaxation peaks, with the maximum values shifting toward higher frequencies as the temperature increases. The frequency ranges to the left of the peaks correspond to long-range movements of mobile ions. On the other hand, the frequency ranges to the right of the peaks correspond to ions that are more confined within their potential wells.

The frequency at which the maximum of the relaxation peaks (M'' max) is observed indicates a transition from short-distance to long-distance movement of charge carriers as the frequency decreases.[70] We noticed that the change in the maximum value of M'' with temperature reflects a variation in capacitance. Besides, the asymmetrical broadening of the peak, indicating non-Debye-type conduction behavior, signifies the transmission of relaxation phenomena within the material.[69]

3.4.4. Dielectric Measurement. To gain a deeper understanding of the material's response to electric fields and confirm the phase transitions observed in the thermal and electrical analyses, we carefully examine the variation of the permittivity. This investigation provides invaluable insights into a wide range of material properties, including ion flow, relaxation time, and electrical conductivity, within the studied material.

The real (ε') and imaginary (ε'') parts of the permittivity were determined using the following equations:[71]

$$\varepsilon^* = \varepsilon' r + i\varepsilon r'' \quad (10)$$

$$\varepsilon' = \frac{-Z''}{\omega C_0 (Z'^2 + Z''^2)} \quad (11)$$

$$\varepsilon'' = \frac{-Z'}{\omega C_0 (Z'^2 + Z''^2)} \quad (12)$$

Figure 11a,b illustrates the temperature dependence of the real part (ε') and imaginary part (ε'') of the complex dielectric response (ε^*) for the Ni(II)-based compound at different frequencies. The plots clearly show that the compound undergoes a phase transition at a temperature consistent with the findings from thermal and electrical analyses.

https://doi.org/10.1021/acsomega.3c08499
ACS Omega 2024, 9, 12743−12752

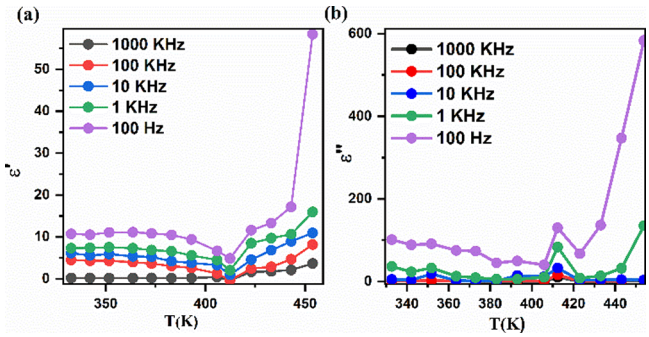

Figure 11. Temperature dependence of (a) the real part (ε') and (b) imaginary part (ε'') for the Ni(II)-based hybrid compound.

Below 413 K, both (ε') and (ε'') remain independent of temperature. However, near the phase transition temperature of 413 K, the real part of the permittivity (ε') exhibits an asymmetric peak, indicating a significant dielectric loss. Simultaneously, the imaginary part of the permittivity (ε'') reaches its maximum at this critical temperature (T_c = 413 K). This anomaly can be attributed to the dynamic disorder of the crystal lattice caused by the reorientation movement of the inorganic chains.[34,37]

The frequency-dependent behavior of the real part of the permittivity (ε') at different temperatures is illustrated in Figure 12a. At low frequencies, it is observed that the

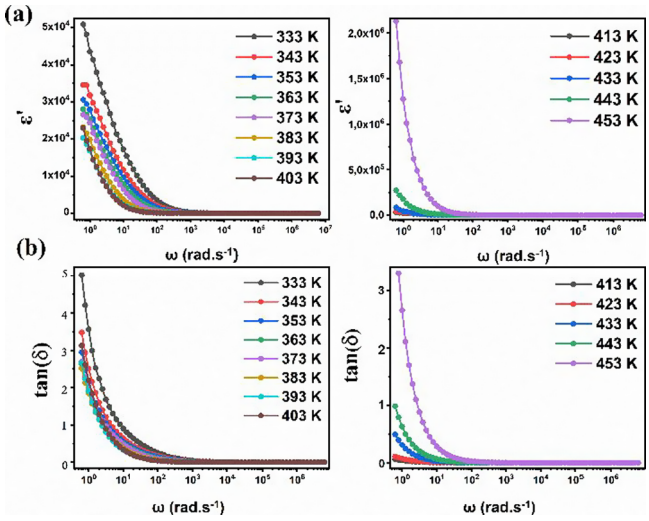

Figure 12. (a) Frequency-dependent on the real part of the permittivity (ε') at different temperatures. (b) The variation of the dissipation factor (tan (δ)) with frequency.

investigated sample exhibits higher (ε') values, reaching 10^4, suggesting its potential as a suitable candidate for low-frequency energy storage applications. As the frequency increases, the (ε') values decrease, indicating an improvement in the energy storage capacity.[37] According to the literature, the dielectric constants of conventional semiconductors, such as inorganic compounds, are significantly lower compared to our investigated compound ($\varepsilon' \sim 10^4$).[72,73] Silicon, for instance, has a dielectric constant of 12.1,[74] while organic semiconductors typically exhibit dielectric constants ranging from 2 to 5. The reported hybrid compound $(C_6H_9N_2)FeCl_4$[34] exhibits substantial dielectric constants, approximately in the range of $\varepsilon \sim 10^6$ at lower frequencies and demonstrates high electrical conductivity and minimal dielectric loss at high frequencies. In fact, higher dielectric constants are associated with increased resistance to electric fields.[34,36] Additionally, materials with high dielectric constants have the potential to enhance the performance of electronic devices. Hence, the high dielectric constant of the Ni(II) halide-based compound makes it suitable for electronic capacitor systems.

The dielectric loss (tan (δ)) is defined as the ratio of the imaginary part of the permittivity (ε") to the real part of the permittivity (ε').[75,76] Various physical phenomena contribute to dielectric loss, including the conduction process, dielectric relaxation, molecular dipole moment, and interfacial polarization.

The variation of the dissipation factor (tan (δ)) with frequency is shown in Figure 12b. The plots exhibit a similar trend to the variation of the real part of the permittivity (ε'), indicating a gradual decrease with increasing temperature and frequency.

In the low-frequency range, a higher amount of energy is required to induce the movement of charge carriers, resulting in higher (tan (δ)) values. However, as the frequency increases, the resistivity of the material decreases, leading to less energy consumption for charge carrier movement. Consequently, the dielectric loss decreases in the high-frequency region. These observations suggest that the investigated perovskite material has potential for use in electrical devices specially in the field of electronic capacitors.[77]

4. CONCLUSIONS

In conclusion, a low-dimensional semiconducting Ni(II)-based hybrid compound with promising optical and electrical properties has been synthesized and extensively characterized through various techniques. The monoclinic structure packing revealed infinite layers comprising organic rings and inorganic $[NiCl_4]^{2-}$ tetrahedral, both linked by intermolecular hydrogen bonds, conferring a 2D framework. A deep investigation of the optical properties revealed an optical band gap energy of 2.6 eV, confirming the semiconductor nature of the investigated material. This finding highlights its potential for optoelectronic applications and light absorption properties, which are particularly significant for achieving high energy conversion efficiency in solar cells. The electric and dielectric properties of this material, including its high dielectric permittivity, high conductivity, and low dielectric loss, underscore its potential as an excellent material for electronic capacitors. Based on these results, we strongly believe that the research findings pave the way toward the design of novel halide-based hybrid materials that hold great promise as environmentally friendly alternatives for optical and electronic capacitor devices, potentially contributing to sustainable and cleaner technologies.

■ ASSOCIATED CONTENT

Data Availability Statement

Supplementary crystallographic data for this article are available as electronic supplementary publication from Cambridge Crystallographic Data Centre (CCDC: 2246385). This data can be obtained free of charge via https://www.ccdc.cam.ac.uk/community/deposita structure/CSD Communications/, or from the Cambridge Crystallographic Data Centre, 12 Union Road, Cambridge CB2 1EZ, UK (Fax: (international): + 441223/336033; email: deposit @ ccdc.cam.ac.uk.

https://doi.org/10.1021/acsomega.3c08499
ACS Omega 2024, 9, 12743−12752

Supporting Information

The Supporting Information is available free of charge at https://pubs.acs.org/doi/10.1021/acsomega.3c08499.

Crystallographic tables and asymmetric unit of the ($C_7H_{12}N_2$) $NiCl_4$ title compound (PDF)

AUTHOR INFORMATION

Corresponding Author

Zakaria Elaoud − *Laboratory Physical-Chemistry of Solid State, University of Sfax, Faculty of Sciences of Sfax, 3018 Sfax, Tunisia*; Email: zakaria.elaoud@fss.usf.tn

Authors

Dhouha Abid − *Laboratory Physical-Chemistry of Solid State, University of Sfax, Faculty of Sciences of Sfax, 3018 Sfax, Tunisia*; orcid.org/0000-0002-5967-5876

Issam Mjejri − *Unit of Materials and Environment (UR15ES01), IPEIT, University of Tunis, 1089 Montfleury, Tunisia*

Abderrazek Oueslati − *Laboratory of Spectroscopic Characterization and Optical Materials, Faculty of Sciences, University of Sfax, Sfax 3000, Tunisia*; orcid.org/0000-0002-3221-3401

Philippe Guionneau − *Univ. Bordeaux, CNRS, Bordeaux INP, ICMCB, UMR 5026, F-33600 Pessac, France*

Stanislav Pechev − *Univ. Bordeaux, CNRS, Bordeaux INP, ICMCB, UMR 5026, F-33600 Pessac, France*

Nathalie Daro − *Univ. Bordeaux, CNRS, Bordeaux INP, ICMCB, UMR 5026, F-33600 Pessac, France*

Complete contact information is available at: https://pubs.acs.org/10.1021/acsomega.3c08499

Author Contributions

All authors contributed to the discussions and revisions of the manuscript. D.A.: characterization, writing, original draft, methodology, data curation, and conceptualization. I.M.: conceptualization, characterization, writing, and validation. A.O.: original draft and data curation. P.G.: validation and supervision. S.P.: validation and supervision. N.D.: validation and supervision. Z.E.: supervision, review, and methodology.

Notes

The authors declare no competing financial interest.

ACKNOWLEDGMENTS

A great thanks to ICMCB Bordeaux France, especially the XR diffraction service.

REFERENCES

(1) Zhou, L.; Tian, J.; Liu, S.; Mai, R.; Fu, L.; Madawala, U. K. High-Efficiency WPT Systems for Potable Electronics Based on DC-Bias-Voltage-Controlled Variable Capacitor. *IEEE Trans. Ind. Electron.* **2023**, *71*, 4707.

(2) Yao, B.; Zhang, Y.; Correia, P.; Wu, R.; Song, S.; Trintis, I.; Wang, H.; Wang, H. Accelerated Degradation Testing and Failure Phenomenon of Metalized Film Capacitors for AC Filtering. In *2023 IEEE Applied Power Electronics Conference and Exposition (APEC)*; IEEE, 2023−March; pp. 1846−1850.

(3) Liu, Y.; Shang, S.; Mo, S.; Wang, P.; Wang, H. Eco-Friendly Strategies for the Material and Fabrication of Wearable Sensors. *Int. J. Precis. Eng. Manuf. - Green Technol.* **2021**, *8* (4), 1323−1346.

(4) Li, H.; Zhou, S.; Zhao, J.; Yan, T.; Du, Y.; et al. Dielectric Temperature Stability and Energy Storage Performance of NBT-Based Lead-Free Ceramics for Y9P Capacitors. *J. Adv. Dielectric.* **2023**, *13* (1), No. 2242007, DOI: 10.1142/S2010135X22420073.

(5) Chung, D. D. L.; Xi, X. Introducing Solder-Based Electronics, with Solder Functioning as Resistor, Capacitor, and Power Source. *J. Mater. Sci. Mater. Electron.* **2023**, *34* (2), 1−16.

(6) Binari, M.; Lokhande, A. C.; Almarzooqi, F.; Choi, D. MnO2 nanotube/GO composite anode for high performance lithium-ion capacitor. *J. Power Sources Adv.* **2023**, *24*, No. 100130, DOI: 10.1016/j.powera.2023.100130.

(7) Ma, Y.; Hou, C.; Kimura, H.; Xie, X.; Jiang, H.; Sun, X.; Yang, X. Recent Advances in the Application of Carbon - Based Electrode Materials for High - Performance Zinc Ion Capacitors: A Mini Review. *Adv. Compos. Hybrid Mater.* **2023**, *6* (2), 59.

(8) Ye, F.; Tang, X. G.; Ge, P. Z.; Jiang, Y. P.; Liu, Q. X. BaTiO3-Based Ferroelectric Thin Film Capacitor on Silicon for Ultra-High Energy Storage Performance at Low Electric Field Strength. *IEEE Electron. Device Lett.* **2023**, *44*, 1376.

(9) Singh, K.; Sharma, S.; Singh, B.; Gupta, M.; Tripathi, C. C. Fabrication of graphene, graphite and multi wall carbon nano tube based thin films and their potential application as strain sensor. *Thin Solid Films.* **2022**, *761*, No. 139540.

(10) Velpula, G.; Lian, J. X.; Cornil, D.; Beljonne, D.; Lazzaroni, R.; Mali, K. S.; De Feyter, S. Ionic Liquid−Graphene Interface: Effect of Anions on the Fermi Level. *J. Phys. Chem. C* **2023**, *127*, 12717.

(11) Lee, Y. B.; Ahn, S.; Kim, D. W.; Song, Y. H.; Kim, Y. C. Ultra-Compact Free-Electron Laser Advanced Model for Carbon Nano-Tube Tip. *Appl. Sci. Converg. Technol.* **2023**, *32* (3), 58−62.

(12) Sahoo, S.; Satpati, A. K. Determination of Curcumin on Functionalized Carbon Nano Tube Modified Electrode and Probing its Interaction with DNA and Copper Ion. *J. Anal. Test.* **2023**, *7* (2), 136−146.

(13) Smaoui, S.; Aribia, W. Ben; Kabadou, A.; Abdelmouleh, M. X-ray powder diffraction, spectroscopic study, dielectric properties and thermal analysis of new doped compound TiGa0. 67Te2. 33O8. *J. Mol. Struct.* **2016**, *1133*, 422 DOI: 10.1016/j.molstruc.2016.11.072.

(14) Khalfa, M.; Oueslati, A.; Khirouni, K.; Gargouri, M.; Rousseau, A.; Lhoste, J.; Bardeau, J. F.; Corbel, G. Synthesis, Structural and Electrical Characterization of a New Organic Inorganic Bromide: [(C3H7)4N]2CoBr4. *RSC Adv.* **2022**, *12* (5), 2798−2809.

(15) Nicholas, A. D.; Halli, R. N.; Garman, L. C.; Cahill, C. L. Low-Dimensional Hybrid Indium/Antimony Halide Perovskites: Supramolecular Assembly and Electronic Properties. *J. Phys. Chem. C* **2020**, *124* (47), 25686−25700.

(16) Wang, P.; Wang, H.; Ye, F.; Zhang, H.; Chen, M.; Cai, J.; Li, D.; Liu, D.; Wang, T. Contrasting Effects of Organic Chloride Additives on Performance of Direct and Inverted Perovskite Solar Cells. *ACS Appl. Mater. Interfaces* **2019**, *11* (41), 37833−37841.

(17) Dhahri, A.; Dhahri, E.; Hlil, E. K. Electrical conductivity and dielectric behaviour of nanocrystalline La 0.6 Gd 0.1 Sr 0.3 Mn 0.75 Si 0.25 O 3. *RSC Adv.* **2018**, *8*, 9103−9111.

(18) Gzaiel, M. Ben; Oueslati, A.; Hlel, F.; Gargouri, M. Synthesis, Crystal Structure, Phase Transition and Electrical Conduction Mechanism of the New [(C3H7)4N]2MnCl4 Compound. *Physica E* **2016**, *83*, 405−413.

(19) Moutia, N.; Oueslati, A.; Ben Gzaiel, M.; Khirouni, K. Crystal Structure and AC Conductivity Mechanism of [N(C3H7)4]2CoCl4 Compound. *Phys. E Low-Dimensional Syst. Nanostructures* **2016**, *83*, 88−94.

(20) Abid, D.; Dhouib, I.; Guionneau, P.; Pechev, S.; Chaabane, I.; Daro, N.; Elaoud, Z. Proton Conduction Study of a New Selenate-Based Hybrid Compound. *J. Alloys Compd.* **2020**, *824*, No. 153826.

(21) Dhouib, I.; Abid, D.; Ouasri, A.; Guionneau, P.; Elaoud, Z. DFT Computation, Hirshfeld Surfaces Analysis, Non-Linear Optical and Spectroscopic Investigations of a Novel Non-Centrosymmetric Organic − inorganic Hybrid Material [(CH3CH2)4N]HSeO4-(H2SeO4)2. *J. Solid State Chem.* **2021**, *299* (March), No. 122134.

(22) Yangui, A.; Roccanova, R.; McWhorter, T. M.; et al. Hybrid Organic−Inorganic Halides (C5H7N2)2MBr4 (M = Hg, Zn) with

High Color Rendering Index and High-Efficiency White-Light Emission. *Chem. Mater.* **2019**, *31* (100), 2983−2991.
(23) Liu, K.; Jiang, Y.; Jiang, Y.; Guo, Y.; Liu, Y.; Nakamura, E. Chemical Formation and Multiple Applications of Organic-Inorganic Hybrid Perovskite Materials. *J. Am. Chem. Soc.* **2019**, *141* (4), 1406−1414.
(24) Han, C.; Bradford, A. J.; Slawin, A. M. Z.; Bode, B. E.; Fusco, E.; Lee, S. L.; Tang, C. C.; Lightfoot, P. Structural Features in Some Layered Hybrid Copper Chloride Perovskites: ACuCl4or A2CuCl4. *Inorg. Chem.* **2021**, *60* (15), 11014−11024.
(25) Bourwina, M.; Msalmi, R.; Walha, S.; Turnbull, M. M.; Roisnel, T.; Costantino, F.; Mosconi, E.; Naïli, H. A New Lead-Free 1D Hybrid Copper Perovskite and Its Structural, Thermal, Vibrational, Optical and Magnetic Characterization. *J. Mater. Chem. C* **2021**, *9* (18), 5970−5976.
(26) Akrout, F.; Hajlaoui, F.; Karoui, K.; Audebrand, N.; Roisnel, T. Two-Dimensional Copper (II) Halide-Based Hybrid Perovskite Templated by 2-Chloroethylammonium: Crystal Structures, Phase Transitions, Optical and Electrical Properties. *J. Solid State Chem.* **2020**, *287*, No. 121338.
(27) Abid, D.; Abid, H.; Maalej, W.; Hlil, E.; Guionneau, P.; Pechev, S.; Daro, N.; Elaoud, Z. A 1D Helical Eco-Friendly Mn(II) Halide Coordination Polymer: Luminescent Properties Involving Resonant Energy Transfer and Magnetic Characterization. *J. Lumin.* **2022**, *252* (July), No. 119251.
(28) Barkaoui, H.; Abid, H.; Yangui, A.; Triki, S.; Boukheddaden, K.; Abid, Y. Yellowish White-Light Emission Involving Resonant Energy Transfer in a New One-Dimensional Hybrid Material: (C9H10N2)-PbCl4. *J. Phys. Chem. C* **2018**, *122* (42), 24253−24261.
(29) Barkaoui, H.; Abid, H.; Zelewski, S.; Urban, J.; Baranowski, M.; Mlayah, A.; Triki, S.; Plochocka, P.; Abid, Y. Negative Thermal Quenching of Efficient White-Light Emission in a 1D Ladder-Like Organic/Inorganic Hybrid Material. *Adv. Opt. Mater.* **2019**, *7*, No. 1900763, DOI: 10.1002/adom.201900763.
(30) Creason, T. D.; Yangui, A.; Roccanova, R.; Strom, A.; Du, M. Rb 2 CuX3 (X = Cl, Br): 1D All-Inorganic Copper Halides with Ultrabright Blue Emission and Up-Conversion Photoluminescence. *Adv. Opt. Mater.* **2019**, *8*, No. 1901338, DOI: 10.1002/adom.201901338.
(31) Elleuch, S.; Lusson, A.; Pillet, S.; Boukheddaden, K.; Abid, Y. White Light Emission from a Zero-Dimensional Lead Chloride Hybrid Material. *ACS Photonics* **2020**, 7 (5), 1178−1187.
(32) Yangui, A.; Roccanova, R.; McWhorter, T.; et al. Hybrid Organic−Inorganic Halides (C5H7N2)2MBr4 (M = Hg, Zn) with High Color Rendering Index and High-Efficiency White-Light Emission. *Chem. Mater.* **2019**, *31* (100), 2983−2991.
(33) Yangui, A.; Roccanova, R.; Wu, Y.; Du, M.; Saparov, B. Highly E Ffi Cient Broad-Band Luminescence Involving Organic and Inorganic Molecules in a Zero-Dimensional Hybrid Lead Chloride. *J. Phys. Chem. C* **2019**, *123*, 22470−22477.
(34) Ghoudi, A.; Ben Brahim, K.; Ghalla, H.; Lhoste, J.; Auguste, S.; Khirouni, K.; Aydi, A.; Oueslati, A. Crystal Structure and Optical Characterization of a New Hybrid Compound, C6H9N2FeCl4, with Large Dielectric Constants for Field-Effect Transistors. *RSC Adv.* **2023**, *13* (19), 12844−12862.
(35) Khawla, M.; Dhouha, A.; Ikram, D.; Slim, E.; Ali, O.; Zakaria, E. A 0D lead-free Nickel halide-based perovskite exhibiting greenish light emission and high color rendering index. *Mater. Res. Bull.* **2023**, *167*, No. 112396.
(36) Hamdi, I.; Mhadhbi, N.; Issaoui, N.; El-Ghozzi, M.; Tozri, A.; Naïli, H. Experimental and theoretical investigations on structural-function relationship of new iron (III) complex with 2-(Ammonio-methyl) pyridinium cation as ligand: A promising material for green solar cells. *J. Mol. Struct.* **2022**, *1251*, No. 132051.
(37) Kalthoum, R.; Bechir, M. B.; Rhaiem, A. B.; Dhaou, M. H. Optical properties of new organic-inorganic hybrid perovskites (CH3) 2NH2CdCl3 andCH3NH3CdCl3 for solar cell applications. *Opt. Mater.* **2022**, *125*, No. 112084.
(38) Sheldrick, G M. *SHELXL-97, Program of X-ray Crystallographic Structure Refinement*; Gottingen Univ.: Gottingen, Germany, 1997.
(39) Farrugia, L. J. WinGX suite for small-molecule single-crystal crystallography. *J. Appl, Crystallogr.* **1999**, *32*, 837.
(40) Sheldrick, G. M. *SHELXL-2018/1, Program for Crystal Structure Refinement*; University of Göttingen: Germany, 2018.
(41) Brandenburg, K. *Diamond Version 4, 0*; Impact GbR: Bonn, Germany. 2009.
(42) Gerdes, A.; Bond, M. R. Octakis (dimethylammonium) hexa-μ2-chlorido-hexachloridotrinickelate (II) dichloride: a linear trinickel complex with asymmetric bridging. *Acta Crystallogr. C* **2009**, *65*, m398−m400, DOI: 10.1107/S0108270109036853.
(43) Laine, T. V; Piironen, U.; Lappalainen, K.; Klinga, M.; Aitola, E. Pyridinylimine-Based Nickel (II) and Palladium (II) Complexes: Preparation, Structural Characterization and Use as Alkene Polymerization Catalysts. *J. Organomet. Chem.* **2000**, *606*, 112−124, DOI: 10.1016/S0022-328X(00)00291-6.
(44) Zhang, Y.; Du, M.; La, Y.; Yan, Y.; Dong, W. Synthesis, Structural Characterizations and Theoretical Calculations of the Ni(II) Complex Based on a Novel Salamo-Salen-Salamo-Type Hybrid Ligand. *J. Mol. Struct.* **2024**, *1296*, No. 136841, DOI: 10.1016/j.molstruc.2023.136841.
(45) Salah, B.; Walha, S.; et al. Crystal Growth, Thermal and Magnetic Characterizations of a New Ferromagnetic Ni(II) Dimer. *Monatsh. Chem.* **2014**, *145*, 1575−1581.
(46) Baur, W. H. The Geometry of Polyhedral Distortions. Predictive Relationships for the Phosphate Group. *Acta Crystallographica Section B: Structural Crystallography and Crystal Engineering and Materials.* **1974**, *30*, 1195−1215.
(47) Kekeç, S.; Süheyla, G.; Okan, K.; Yeşilel, Z.; Şahin, O. Syntheses, Crystal Structures, Spectroscopic and Thermal Properties of 3D Heteronuclear Coordination Polymers with 4 - Ethylpyridine and Cyanide Ligands. *Struct. Chem.* **2023**, DOI: 10.1007/s11224-023-02249-2.
(48) Kürkçüoğlu, G. S.; Yeşilel, O. Z.; et al. Synthesis, Crystal Structure and Spectroscopic Investigations of Heteronuclear Co (III)/ Cu (II), Co (III)/ Cd (II) and Fe (III)/ Cd (II) 3D Coordination Polymers with 4-(2-Aminoethyl) Pyridine. *J. Mol. Struct.* **2023**, *1274*, No. 134540, DOI: 10.1016/j.molstruc.2022.134540.
(49) Brewer, G. Structural Evidence of Spin State Selection and Spin Crossover Behavior of Tripodal Schi Ff Base Complexes of Tris (2-Aminoethyl) Amine and Related Tripodal Amines. *Magnetochemistry* **2020**, *6*, 28 DOI: 10.3390/magnetochemistry6020028.
(50) Said, M.; Boughzala, H. Synthesis, crystal structure, vibrational study, optical properties and thermal behavior of a new hybrid material bis(3-amino-4-phenyl-1H-pyrazolium) tetrachloridocobaltate (II) monohydrate. *J. Mol. Struct.* **2020**, *1203*, No. 127413.
(51) Essid, M.; Aloui, Z.; Ferretti, V.; Abid, S.; Lefebvre, F.; Rzaigui, M.; Nasr, B. C. Crystal structure, Hirshfeld surface and spectroscopic studies of the noncentrosymmetric Bi(III) halide complex: [C8H12N]3BiCl6. *J. Inorg. Chim. Acta* **2017**, *457*, 122−129.
(52) Braga, D.; Grepioni, F.; Maini, L.; Mazzeo, P. P.; Ventura, B. Solid-state reactivity of copper(i) iodide: luminescent 2D-coordination polymers of CuI with saturated bidentate nitrogen bases. *New J. Chem.* **2011**, *35*, 339−344.
(53) Aydi, S.; Chkoundali, S.; Oueslati, A.; Aydi, A. Effect of lithium doping on the structural, conduction mechanism and dielectric property of MnNbO 4. *RSC Adv.* **2023**, *13*, 20093−20104, DOI: 10.1039/D3RA03393G.
(54) Ateş, A.; brahim, K. B.; et al. Investigation of Structural, Morphology, and Conduction Mechanism of GO−Fe $_3O_4$−TiO2 Composite Material. *J. Mater. Sci.* **2023**, *34*, 1703 DOI: 10.1007/s10854-023-11126-x.
(55) Medhioub, O.; Samet, A.; Barkaoui, H.; Triki, S.; Abid, Y. Multiexcitonic Broad-Band Emission Enhanced by Resonant Energy Transfer in a New Two-Dimensional Organic − Inorganic Perovskite: $(C_3H_8N_6)PbCl_4$. *J. Phys. Chem. C* **2020**, *124*, 20359 DOI: 10.1021/acs.jpcc.0c04768.

https://doi.org/10.1021/acsomega.3c08499
ACS Omega 2024, 9, 12743−12752

(56) Samet, A.; Pillet, S.; Abid, Y. Sensitizer-Free Photon up Conversion in (HQ)2ZnCl4 and HQCl Crystals: Systems Involving Resonant Energy Transfer and Triplet-Triplet Annihilation. *Phys. Chem. Chem. Phys.* **2020**, *22* (3), 1575−1582.
(57) Yangui, A.; Roccanova, R.; McWhorter, T. M.; et al. Hybrid Organic−Inorganic Halides (C5H7N2)2MBr4 (M = Hg, Zn) with High Color Rendering Index and High-Efficiency White-Light Emission. *Chem. Mater.* **2019**, *31*, 2983−2991.
(58) Maalej, W.; Hajlaoui, F.; Karoui, K.; Audebrand, N.; Roisnel, T. Crystal structure and semiconductor properties of copper (II) complex incorporating chiral (R)-(+)-α-Ethylbenzylammonium cations:[(R)-C9H14N] 3 [CuBr4]. *Br. Journal of Solid State Chemistry.* **2022**, *305*, No. 122646.
(59) Dakhlaoui, I.; Karoui, K.; Hajlaoui, F.; et al. A new supramolecular semiconductor palladium (ii) complex [(CH 3) 3 N (CH 2) 3 Br] 2 Pd 2 Cl 6: structural study, optical and electrical properties. *New J. Chem.* **2023**, *47* (17), 8042−8049.
(60) Trabelsi, K.; Karoui, K.; Hajlaoui, F.; et al. An organic-inorganic hybrid cadmium chloride with face-sharing CdCl6 octahedral chains: Synthesis, crystal structure, optical and conduction mechanisms: [NH2 (CH3) 2] 5Cd3Cl11. *Opt. Mater.* **2022**, *134*, No. 113100, DOI: 10.1016/j.optmat.2022.113100.
(61) Ben Mohamed, C.; Karoui, K.; Tabellout, M.; Ben Rhaiem, A. Electrical, Dielectric and Optical Properties of [C2H5NH3]-2ZnCl4compound. *J. Alloys Compd.* **2016**, *688*, 407−415.
(62) Weslati, N.; Gzaiel, M. B.; Chaabane, I.; Hlel, F. Ionic Conduction Mechanism and Relaxation Studies of NaNbAlP3O12 Compound. *Ionics* **2018**, *24* (1), 181−188.
(63) Ben Nasr, W.; Kchaou, H.; Ben Rhaiem, A. Phase Transition and Conduction Mechanism Study by Overlapping Large-Polaron Tunnelling Model in Li2MoO4 Ceramic Compound. *Phys. E Low-Dimensional Syst. Nanostructures* **2018**, *102*, 110−116.
(64) Ben Mohamed, C.; Karoui, K.; Bulou, A.; Ben Rhaiem, A. Electrical Properties and Raman Studies of Phase Transitions in Ferroelectric [N(CH3)4]2CoCl2Br2. *Phys. E Low-Dimensional Syst. Nanostructures* **2018**, *97*, 136−143.
(65) Kulkarni, S.; Nagabhushana, B. M.; Parvatikar, N.; Koppalkar, A.; Shivakumara, C.; Damle, R. Dielectric and Electrical Studies of Pr 3 + Doped Nano CaSiO 3 Perovskite Ceramics. *Mater. Res. Bull.* **2014**, *50*, 197−202.
(66) Howell, F. S.; et al. Electrical relaxation in a glass-forming molten salt. *J. Phys. Chem.* **1988**, *38* (14), 639−648.
(67) Bishop, A. R.; et al. Breathers and photoinduced absorption in polyacetylene. *Phys. Rev. Lett.* **1984**, *52* (8), 671−674.
(68) Slima, I. B.; Karoui, K.; Rhaiem, A. B. Ionic Conduction, Structural and Optical Properties of LiCoO 2 Compound. *Ionics* **2023**, *29*, 1731 DOI: 10.1007/s11581-023-04960-w.
(69) Krimi, M.; Karoui, K.; Suñol, J. J.; Ben Rhaiem, A. Phase Transition, Impedance Spectroscopy and Conduction Mechanism of Li0.5Na1.5WO4Material. *Phys. E Low-Dimensional Syst. Nanostructures* **2018**, *102*, 137−145.
(70) Nobre, M. A.; Lanfredi, S. Dielectric Spectroscopy on Bi 3 Zn 2 Sb 3 O 14 Ceramic: An Approach Based on the Complex Impedance. *J. Phys. Chem. Solids* **2003**, *64*, 2457−2464, DOI: 10.1016/j.jpcs.2003.08.007.
(71) Missaoui, F.; et al. Structural, dielectric and transport properties of NaxFe1/2Mn1/2O2 (x = 1 and 2/3). *RSC Adv.* **2023**, *13* (26), 17923−17934.
(72) Khopkar, V.; Sahoo, B. Low Temperature Dielectric Properties and NTCR Behavior of the BaFe0.5Nb0.5O3 Double Perovskite Ceramic. *Phys. Chem. Chem. Phys.* **2020**, *22* (5), 2986−2998.
(73) Hossain, K.; Singh, S.; Kabra, D. Role of Monovalent Cations in the Dielectric Relaxation Processes in Hybrid Metal Halide Perovskite Solar Cells. *ACS Appl. Energy Mater.* **2022**, *5* (3), 3689−3697.
(74) Kingon, A. I.; Maria, J. P.; Streiffer, S. K. Alternative dielectrics to silicon dioxide for memory and logic devices. *Nature* **2000**, *406*, 1032−1038.
(75) Gharbi, I.; Oueslati, A.; Ates, A.; Mahmoud, A.; Zaghrioui, M.; Gargouri, M. RSC Advances Investigation of Structural, Morphological, and. *RSC Adv.* **2023**, *13*, 10036−10050.
(76) Drissi, N.; et al. Vibrational Spectroscopy, Electrical, and Thermal Properties. *Appl. Organomet. Chem.* **2022**, *36*, No. e6621, DOI: 10.1002/aoc.6621.
(77) Slima, I. B.; Karoui, K.; Khirouni, K.; Mahmoud, A. Investigation of the Optical and Dielectric Properties of NaCu0. 2Fe0. 8- Investigation of the Optical and Dielectric Properties of NaCu 0. 2 Fe 0. 8-X Mn X O 2. *Inorg. Chem. Commun.* **2023**, *157*, No. 111444, DOI: 10.1016/j.inoche.2023.111444.

https://doi.org/10.1021/acsomega.3c08499
ACS Omega 2024, 9, 12743−12752